Residual-moveout-based wave-equation migration velocity analysis — field data example

Yang Zhang and Biondo Biondi

ABSTRACT

We apply our residual-moveout-based (RMO-based) wave-equation migration velocity analysis (WEMVA) method to an industry scale 3-D marine streamers wide-azimuth data set — E-Octopus III in the Gulf of Mexico. This 3-D field data set poses many challenges for our implementation, including irregular geometry, abnormal traces, complex 3-D salt geometry, and more importantly, huge data volume and large domain dimensions. To overcome these hurdles, we apply careful data regularization and preprocessing, and employ a target-oriented inversion scheme that focuses on the update of sediment velocities in specific regions of interest. Such target-oriented scheme significantly reduces the computational cost, allowing us to make our WEMVA method affordable on our academic cluster. Our experiment result on a subsalt sediments target region shows that the angles of illumination on the subsalt sediments are very limited (less than 25 degrees) because of the complex salt overburden and the depth of the target. Although the lack of angular illumination in this region severely reduces the capability of any reflection tomography method that tries to resolve a better velocity model, our RMO-based WEMVA method is still able to detect the curvatures of the angle gathers and produce good velocity model updates that further flatten the angle gathers and improve the quality of the structural image in the target region.

INTRODUCTION

Wave-equation migration velocity analysis (WEMVA) is a reflection tomography method which uses a wave-equation rather than a ray-based model to retrieve the velocity model from seismic data. The velocity information comes from the redundancy in the seismic data, since each reflector point in the subsurface is illuminated by wave energy from multiple directions. WEMVA exploits such redundancy by forming common-image gathers (CIG) and then enforcing coherence among the CIG to improve the velocity model.

We recently proposed a WEMVA method named RMO-based WEMVA (Zhang and Biondi, 2013) that describes the unflatness in the angle-domain common image gathers (ADCIG) using residual-moveout (RMO) parameters. This method tries to improve the velocity model using the moveout information. With the successful

application of the RMO-based WEMVA on 2-D problems such as the 2006 BP synthetic model (Zhang et al., 2013), we have shown that this method does not suffer from cycle-skipping or require the picking of moveout parameters, and it can robustly improve the flatness of the angle gathers.

However, although the theory of this method can be easily extended to 3-D, a realistic 3-D data application remains very challenging. In this study, we examine a marine streamers 3-D wide-azimuth (WAZ) seismic recordings acquired from offshore Gulf of Mexico (GoM) by Schlumberger Multiclient. The remainder of this paper is organized as follows:

- In the first part, we give a brief recap of the 3-D theory of the RMO-based WEMVA. In addition to the basic formulation that assigns a RMO parameter to every image point, we present a refined formulation where the RMO parameters are assigned to individual identified events. In order to support the refined formulation in practical application, we propose the use of several image processing techniques to identify and extract the events in the image.
- In the second part, we focus on the application of our RMO-based WEMVA method on the aforementioned field data set. In the previous report (Zhang and Biondi, 2014), we presented the overview of this WAZ data set, our data preprocessing procedures and the initial 3-D migration images. Here we perform velocity estimation using the RMO-based WEMVA on the data set in a target-oriented manner. The results show improvements in the ADCIG flatness and in the migrated image, which has better defined continuity and coherency in terms of sedimentary structure.

THEORY OF 3-D RMO-BASED WEMVA

In this section, we summarize the theory of the proposed RMO-based WEMVA approach in 3-D. The detailed derivation (refer to Zhang (2015)) is beyond the scope of this paper. Here, we only show key definitions and equations in the method formulation. The model space is parameterized as slowness unless otherwise specified.

In the 3-D case, we denote the prestack image as $I(z, \gamma, \phi, x, y)$, in which (z, x, y) are the depth and horizontal axes, respectively, γ is the reflection opening angle, and ϕ is the subsurface azimuth. Assuming there are m samples along ϕ axis, then $\phi = \{\phi_i : i = 1, 2, ..., m\}$. Let us start from the classical stack-power maximization objective function:

$$J(s) = \frac{1}{2} \sum_{x,y} \sum_{z} \left[\sum_{i} \sum_{\gamma} I(z, \gamma, \phi_i, x, y; s) \right]^2, \tag{1}$$

where s is the model slowness, and $I(z, \gamma, x; s)$ is the prestack image in the reflection-angle domain obtained by migration using the slowness s.

RMO-based WEMVA objective function and its gradient

The objective function defined in equation (1) is known to be prone to the cycle-skipping problem. Recalling that the conventional ray-based reflection tomography does not show such disadvantages, we can approximate objective function (1) at some initial slowness s_0, with an alternative one that focuses on kinematic changes of the ADCIG. Given $I(s_0)$ and $I(s)$ as the prestack images with initial and updated slowness, respectively, we define a residual moveout parameter ρ and its moveout function $\rho \tan^2 \gamma$ that describes (as accurately as possible) the kinematic difference between $I(s)$ and $I(s_0)$. Hence ρ is a function of both s and s_0. Because s_0 will remain fixed during the calculation of the model gradient, we can denote the dependence of ρ simply with $\rho(s)$. We assign independent ρ to the ADCIG at each image point (z, x, y) and each azimuth ϕ_i because there can be many events in the gathers, and each event can have a different moveout.

Next, we replace objective function (1) with one based on normalized moveout semblance:

$$J_{S_m}(\rho(s)) = \sum_{x,y} \sum_{z} \sum_{i} S_m(\rho_i(z,x,y), \phi_i, z, x, y; s_0), \tag{2}$$

in which

$$S_m(\rho_i, \phi_i, z, x, y; s_0) = \frac{\sum_{z_w} \left(\sum_{\gamma} I(z + z_w + \rho_i \tan^2 \gamma, \gamma, \phi_i, x, y; s_0) \right)^2}{\sum_{z_w} \sum_{\gamma} I^2(z + z_w + \rho_i \tan^2 \gamma, \gamma, \phi_i, x, y, ; s_0)}. \tag{3}$$

Maximizing the semblance-based objective function achieves the same goal as maximizing the angle-stack because the optimal model s leads to optimal moveout parameters ρ such that the angle gathers in $I(s_0)$ become flat after being applied the moveout, and flat angle gathers will stack most coherently to yield maximum stacked amplitude. Note that in the above equation, I use a local window of length L for z_w (through this derivation, I assume the summation interval for variable z_w is always $[-L/2, L/2]$). When choosing a value for L, the rule of thumb is that L should not be smaller than the span of the event's wavelet, and it should not be too large such that it contains more than one event in each window.

We use gradient-based methods to solve this optimization problem. The model update given by the gradient of objective function (2) is

$$\frac{\partial J_{S_m}}{\partial s} = \sum_{x,y} \sum_{z} \sum_{i} \frac{\partial \rho_i}{\partial s} \frac{\partial J_{S_m}}{\partial \rho_i}. \tag{4}$$

In the above equation, $\partial \rho / \partial s$ describes the relation between slowness perturbation and moveout parameter perturbation, and $\partial S_m / \partial \rho$ indicates the search for better moveout parameters to flatten the gathers. Without going into the details described in Zhang (2015), we can summarize the calculation of these two terms as follows:

- $\partial J_{S_m} / \partial \rho_i$ is calculated by taking first order derivative along ρ_i on the semblance panel $S_m(\rho_i, \phi_i, z, x, y; s_0)$.

- As for $\partial\rho_i/\partial s$, we can derive a relationship from the moveout perturbation $\Delta\rho$ to the image perturbation ΔI, which is then back-projected into the model space as Δs using the image-space wave-equation tomographic operator.

The global objective function for RMO-based WEMVA

One problem in our RMO-based WEMVA formulation is that it is missing a global objective function. The reason is that the semblance-based objective function (2) is formulated around s_0, the slowness model at the current iteration. Consequently, s_0 will change as the WEMVA method iterates, which makes it difficult to use this objective function as the global objective function for model evaluation. In order to overcome this problem, we propose a global objective function directly based on the semblance (3):

$$J^G_{S_m}(s) = \sum_{x,y}\sum_{z}\sum_{i}\sum_{\rho_i} \rho_i^2 S_m(\rho_i, \phi_i, z, x, y; s). \tag{5}$$

Note that the moveout parameter ρ is simply sweeping through the possible moveout value range and is not associated with model s; in addition, the corresponding inversion aims to minimize instead of maximize equation (5).

The reason we can replace objective function (2) with (5) for easy model evaluation is that the two objective functions aim for the same goal. Equation (2) aims to find the best model s such that the corresponding $\rho(s)$ would flatten the angle gathers $I(s_0)$; this is equivalent to finding the best model s under which the gathers $I(s)$ are all flat. Meanwhile, equation (5) is enforcing the same goal because it penalizes non-zero moveout in $I(s)$, which means that the optimal model it looks for is such that $I(s)$ would have zero moveout everywhere, i.e., be flat.

In summary, the RMO-based WEMVA formulation can be interpreted in the following way: first it defines the global objective function (5) over the moveout semblance of the ADCIG, aiming to flatten all gathers (driving moveout to zero); and then, at every iteration, it approximates the global objective function with equation (2), which yields a superior gradient.

Refined formulation for RMO-based WEMVA using event detection

During the actual implementation of the RMO-base WEMVA, we have noticed a major aspect for improvement. Recalling the gradient calculation in equation (2) and (4), we made an assumption that every image point (in domain (z, x, y)) has an independent moveout parameter ρ. We also assumed the event windows (spanning over z axis) of all reflector events are roughly of equal length and therefore can be summarized with an average event window size L. The main rationale behind making such assumptions is for the simplicity of formulation and coding implementation. However,

assigning ρ for every image point is not only unnecessary but also inconsistent with our method's physical interpretation. Indeed, we should assign moveout parameter ρ to individual events instead of individual image point locations; moreover, we should assign a different window size for each event because there can be large variations of the window sizes among different events.

Switching the assumption from moveout per image point to moveout per event is expected to improve the accuracy of the computed model gradient and also marginally reduce the proposed method's computation cost since it cuts the computation of image perturbation. However, it also brings additional complexity for implementation because now we need to identify individual events in the image gathers.

Automatic event detection

I propose a simple workflow for automatic event detection as follows:

- Our program first detects the center locations of individual events in the zero-offset image $I(z, x, y; s_0)$ as "*anchor points*", instead of blindly assuming that every image sample is its own event.
- For each anchor point detected, the program detects the event width by measuring the event signature (waveform) compactness around the anchor point location.

To avoid clutter, we leave the details of the event detection implementation in the appendix .

Formulation change after introducing event detection

Once we figure out how to do automatic event detection, the modification on our WEMVA formulation becomes simple. We only need to slightly modify the summation indices in the gradient calculation above. Instead of summing over every image point, our method now sums over each identified event anchor point. For example, the semblance-based objective function (2) now becomes

$$J_{S_m}\left(\rho(s)\right) = \sum_{k=1}^{|\mathbf{S_{anchor}}|} \sum_i S_m(\rho_i(z_k, x_k, y_k), \phi_i, z, x, y; s_0), \tag{6}$$

in which $\mathbf{S_{anchor}} = \{(z_k, x_k, y_k)|k = 1, 2, ..., \}$ is the set of event anchor points, and $|\mathbf{S_{anchor}}|$ denotes the size of this set. Similarly, the gradient formula (4) becomes

$$\frac{\partial J_{S_m}}{\partial s} = \sum_{k=1}^{|\mathbf{S_{anchor}}|} \sum_i \frac{\partial \rho_i(z_k, x_k, y_k)}{\partial s} \frac{\partial J_{S_m}}{\partial \rho_i(z_k, x_k, y_k)}. \tag{7}$$

In addition, I change the summation bounds of the local window variable z_w in the semblance formula (3). Originally the bounds are fixed at $[-L/2, +L/2]$, but now the event window sizes are automatically detected on individual bases. These formulation changes are very easy to implement in terms of programming.

RMO-BASED WEMVA ON A 3-D WAZ FIELD DATA SET IN THE GULF OF MEXICO

In this section, we discuss how we apply the RMO-based WEMVA method for subsalt area velocity estimation on the E-Octopus WAZ field data set.

E-Octopus field data set overview

The data set we examine in this report is a WAZ streamer survey acquired offshore Gulf of Mexico (GOM) by Schlumberger. Specifically, it is part of the "E-Octopus phase III" survey in the Green Canyon area. The corresponding survey area is about 35 km by 30 km (inline by cross-line). The offset range of a shot gather is [-4.2 km, +4.2 km] cross-line and $[-7.0\,\text{km}, +7.0\,\text{km}]$ in-line. The recorded data contains $\sim 10,000$ shots, amounting to ~ 11 TB of raw disk space. The recording time per trace is 14 seconds. Please refer to our previous report (Zhang and Biondi, 2014) for more details on the WAZ survey's acquisition setup and our data preprocessing workflow.

Initial migration images on E-Octopus field data set

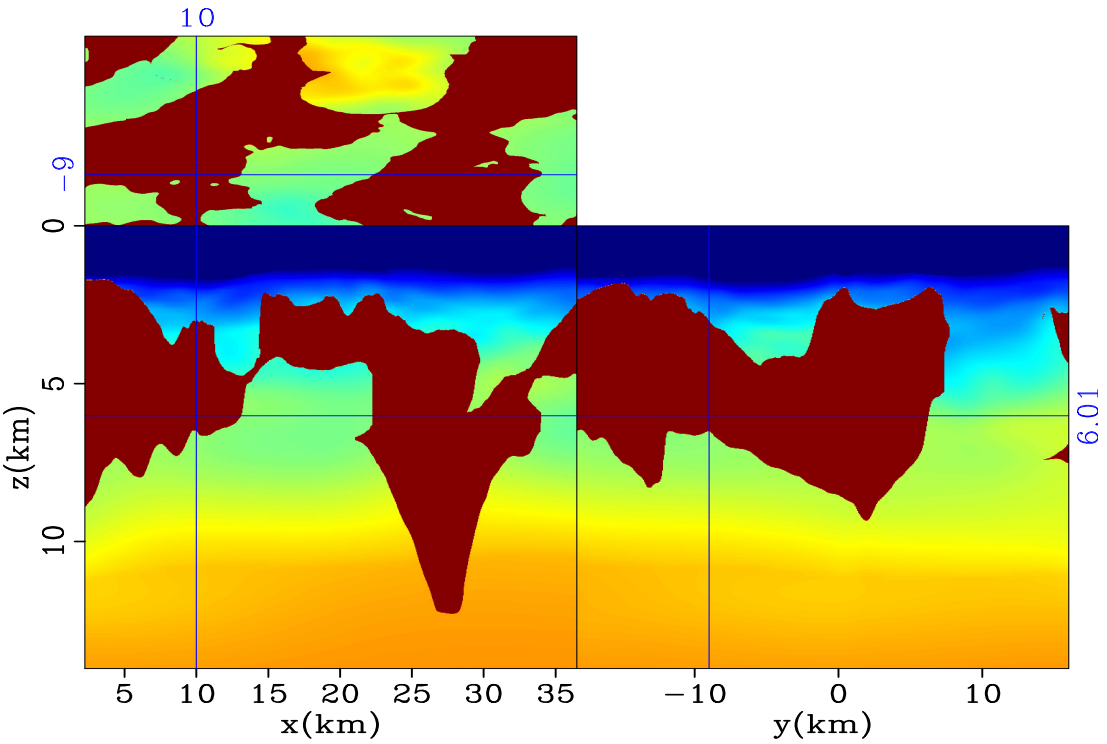

(a)

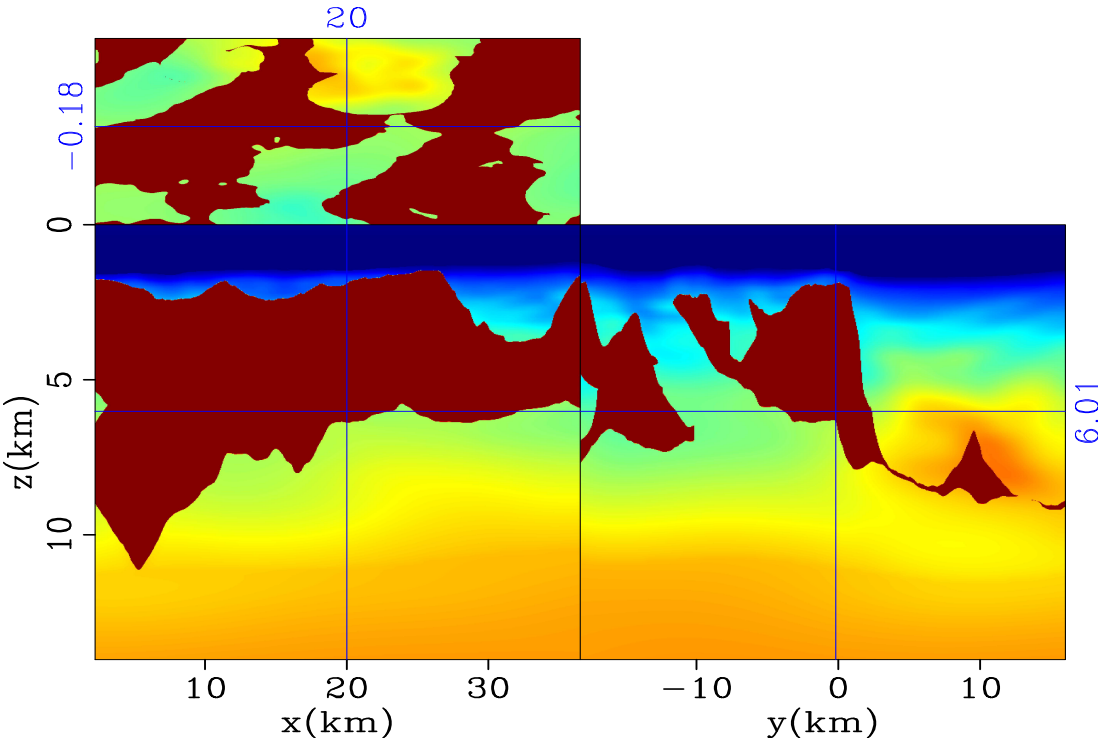

(b)

Figure 1: Three-panel display of the velocity model used for migration. Subplot (a) is sliced at x=10 km,y=−9 km, subplot (b) is sliced at x=20 km,y=−0.99 km. Notice the strong model variations along both X and Y directions. The color map ranges from 1450 m/s (deep blue) to 4480 m/s (deep red). [**ER**]

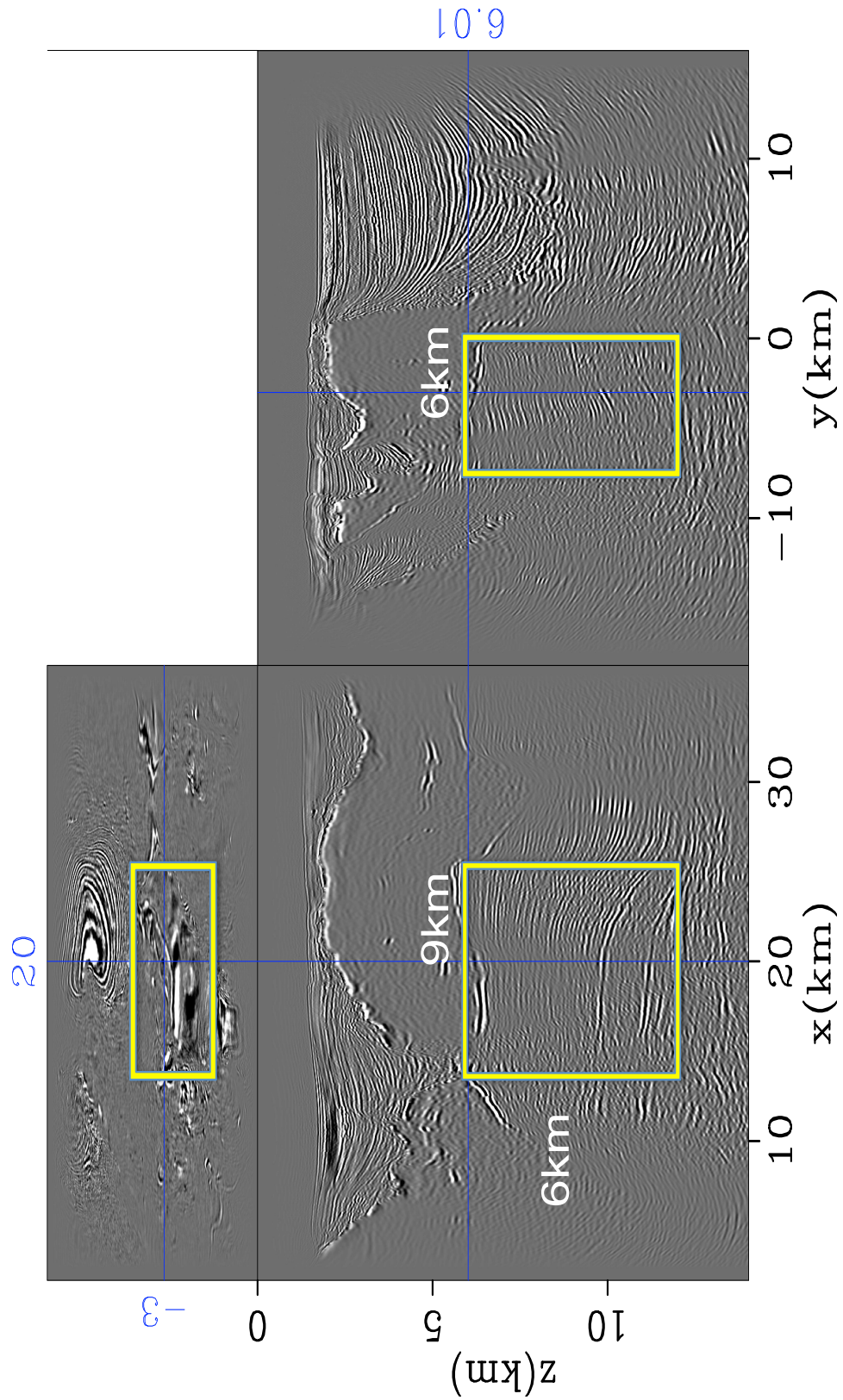

Figure 2: A three-panel view of the initial full 3-D image, in which the region of interest (ROI) for our target-oriented inversion is marked. The image has been applied a z-power (similar to t-power) gain in order to boost up the amplitudes of deeper reflectors. The dimension of ROI is 9 km by 6 km by 6 km. [CR]

Figure 1 shows the best velocity model we received from Schlumberger. The velocity plots show the sections of the same model at different slicing coordinates. As can be seen from figure 1, there are strong lateral variations along both X and Y directions. Figure 2 shows one section of the full 3-D migrated image. As we can see from the figure, the image quality of the sediments above the salt is very good, with continuous and coherent reflector geometries, indicating accurate velocity. However, the subsalt areas are not as well imaged. There are many discontinuities in the reflectors, as well as conflicting dips. We focus our efforts in these regions because of these indications of a less accurate velocity model.

Focusing on subsalt sediments with a target-oriented approach

Applying WEMVA method to a data set at such a large scale will occur prohibitively high computational cost. Even with all the precautions we make in the data preparation stage, a full migration on the entire domain (such as figure 2) costs ∼5000 node×hours on our academic cluster of 120 Intel Xeon nodes (two E5520 CPUs, each CPU is quad-core, 2.26 GHz). It amounts to ~ 50 consecutive hours at 100% cluster usage in the optimal case. In practice, it takes us at least 5 days to complete a job at this scale. The turn-around time would be too long for practical applications, given that the wave-equation tomographic operator is even more expensive than the imaging operator, and that we have to perform tens of iterations in a typical WEMVA inversion. Therefore, to apply expensive wave-equation tomography methods on the target subsalt region, it is essential to adopt a target-oriented approach which greatly shrinks the problem domain, thus significantly reducing the computational cost.

Target-oriented tomography using generalized Born-modeling data

To make the computational cost affordable for our field data application, we use the target-oriented tomography scheme proposed by Tang (2011). This scheme synthesizes a new data set concentrating on the region of interest (ROI), which is able to preserve all kinematic information that is related to the ROI in the original data set. Therefore, in addition to shrinking the problem's physical domain, this scheme reduces the size of the data set used for WEMVA inversion, thus achieving high computational efficiency.

Tang (2011)'s method first computes the initial subsurface offset-domain common-image gathers (ODCIG) in the target region using a starting velocity model. The initial ODCIG are further normalized using the diagonal values of the imaging Hessian, which can be efficiently computed using the phase-encoding method (Tang, 2011), to optimally compensate for the uneven subsurface illumination. Tang (2011) demonstrates that the velocity information about the seismic data is now transformed into the ODCIG. Therefore this method uses the generalized Born modeling method, (which includes the ODCIG instead of merely the zero subsurface offset image in

the modeling process), to simulate a new data set right on top of the target region. The user can design arbitrary acquisition geometry for the synthesized new data set. Once the new data set is generated, the wave-equation tomography is carried out exclusively on the new data set.

The target area we choose is a 9 km by 6 km by 6 km subsalt sediments region near the center of the full imaging domain, as shown in figure 2. Figure 3 shows a close-up view of the velocity and stacked image of the same target region. We consider this area a good target for WEMVA-based velocity improvement because there are a lot of discontinuities among the imaged sediment layer interfaces, which indicates inaccurate medium velocity. Additionally, the salt overburden above this region is relatively well imaged, therefore we have more confidence in the correctness of the overhanging salt model. This leads us to infer that the velocity errors mainly exist within the subsalt sediments, and our WEMVA method is good at resolving these types of velocity errors.

The synthesized new data set

The first step in our target-oriented tomography workflow is to synthesize a data set that sits right on top of the target region while preserving all velocity information around the target region from the original data set. We choose plane-wave acquisition geometry for the new data set because it results in fewer total number of shots that need to be simulated, and the cross-talk effect usually caused by compound sources are kept minimum in plane-wave data. To determine the acquisition parameters of the plane-wave survey, we refer to the fact that the maximum subsurface illumination angle depicted in the ADCIG shown in Zhang and Biondi (2014) is no more than 25°, and the average velocity at the top of the target region is $\sim$ 3000 m/s. The new acquisition samples 17 inlines and 17 crosslines (289 in total) plane-wave directions, with the ray parameters ranging at $\pm$160 us, this corresponds to at least $\pm$30° subsurface angle illumination with $\sim$ 3.75° sampling along angle axis. Because of the reduction of the physical propagation domain, we reduce the recording time from 14.0 secs originally to 6.1 seconds. This translates to coarser sampling in the data frequency domain. Therefore we sample 99 frequencies between 4 Hz and 20 Hz for the new data set, compared to 208 frequencies for the original data set.

We take extra cautions dealing with the salt overburden when synthesizing the new data. First we build a binary mask from the starting velocity model to mark the area occupied by salt in the target region. Then we use this salt mask to erase out the subsurface ODCIG that will be used for the generalized Born modeling because the salt reflection does not provide any velocity information for the sediments below. In addition, as we can see from the velocity model in figure 3(a), over half of the source and receivers in the synthesized survey would be place in salt. The strong lateral variation in the velocity model at the recording depth would cause extra distortion to the plane-wave source wavefields, and it also forces us to use more reference velocities in our one-way propagator, which increases the computational cost. To

address this potential issue, we create a *sediments-flooded* velocity model from the original model in which we replace the salt velocity with the velocity values of its surrounding sediments. We use the salt-excluded subsurface ODCIG combined with the sediments-flooded velocity model to generate our new synthetic data. Figure 4 shows the velocity model and zero subsurface offset section of the ODCIG that we use for the new data synthesis, respectively. We can manipulate the velocity model in this way because the actual salt area is considered not suitable for tomography updates and will remain fixed throughout our velocity estimation workflow. Therefore an ideal way to place the recording locations of the new survey is to put sources and receivers right at the salt/sediment boundary because preserving the sources/receivers wavefields at this boundary will preserve all velocity information about the underlying sediments, but this would cause extra complexity for our one-way propagator implementation. Using the sediments-flooded velocity model avoids such extra complexity because now we can place sources/receivers at the same depth; more importantly, it will preserve the source/receiver wavefields at the salt/sediment boundary since we will not change the part of the velocity model that is originally occupied by salt throughout the tomography workflow.

The mapping from the original data set to this target-oriented plane-wave data set yields huge saving in computation. The size of the data set reduces by 90%, combined with the shrinkage of the modeling physical domain, the required computation time for each migration reduces from 5000 node hours to 150 node hours, a more than 30 times improvement, making overnight calculation per iteration feasible.

To verify that the newly synthesized data set contains the same velocity information as the original data, We recompute the subsurface ODCIG (both in h_x and h_y) using the new data set. In terms of the range of the offset dimensions, we use 21 points in h_x with 50 m spacing and 19 points in h_y with 60 m spacing, in order to capture most of the unfocused energy. The offset dimension is the same as the initial subsurface ODCIG I used to generate the new data set. Figure 5 and figure 6 show the comparison between the gathers migrated using the original data set and the synthesized new data set, respectively. As we can see, except a few disparities close to the boundary, their kinematic behaviors agree with each other very well. Particularly the defocuses and the shapes of the ODCIG are almost identical. Although the long-wavelength amplitude trends are slightly different due to different acquisition geometries, fortunately, our WEMVA inversion algorithm balances the amplitude of the reflectors so that the amplitude variance will not adversely affect the inversion.

Inversion result

We use the Polak-Riberie variant of nonlinear conjugate-gradient (CG) methods to performe the WEMVA iterations. Li (2014) presents a detailed recipe for this algorithm. Based on our empirical observation, we use only half of the data frequencies when applying the wave-equation tomographic operator to further save computation time. In addition, I re-parameterize the model space using coarsely sampled B-spline

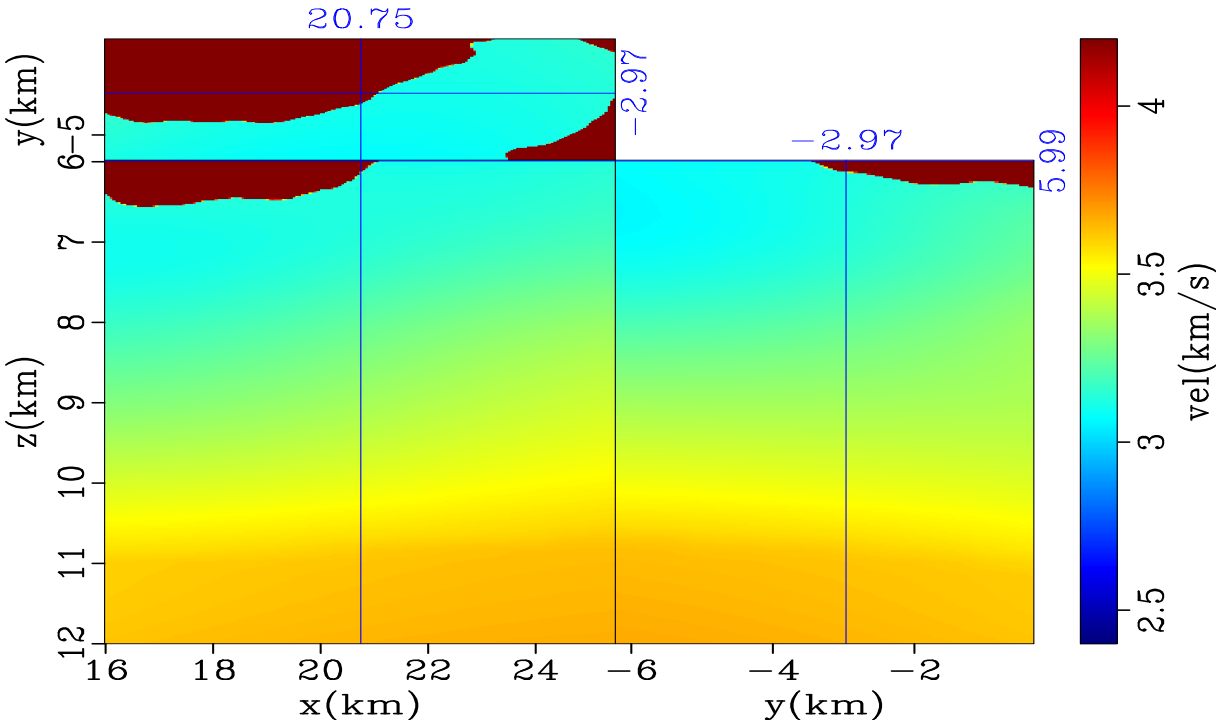

Figure 3: A close-up view of (a) the starting velocity model and (b) the zero subsurface-offset image at the target region (figure 2). [**CR**]

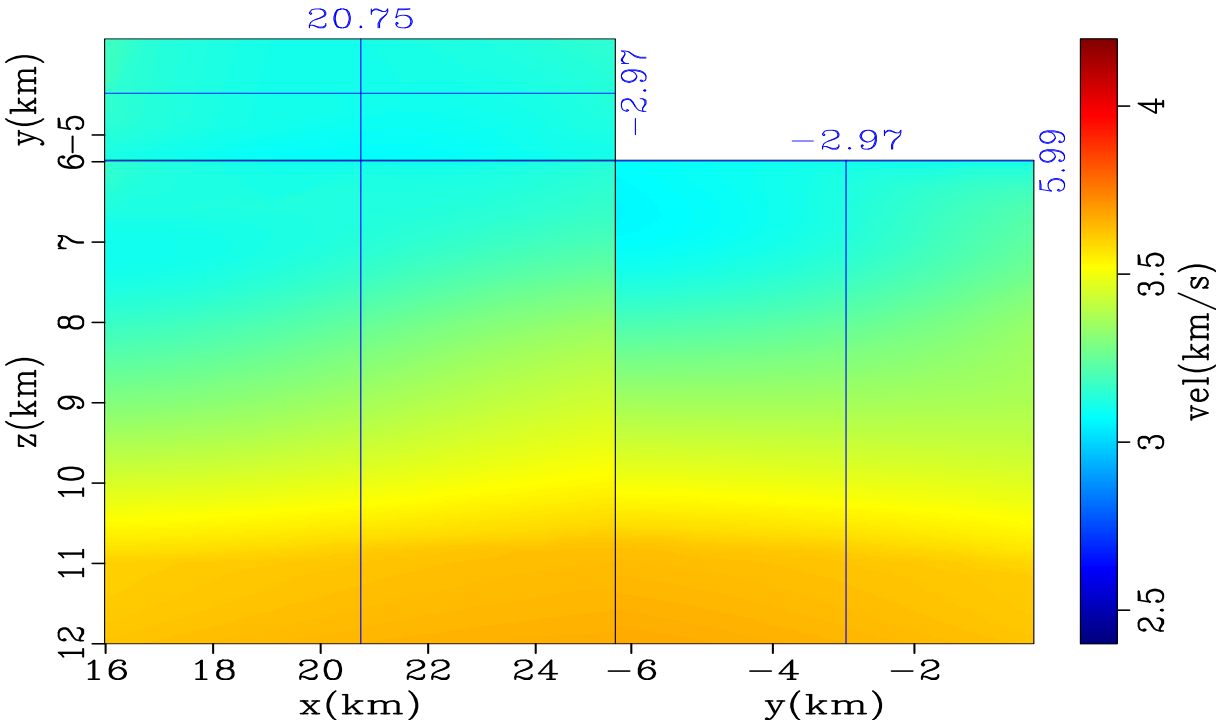

(a)

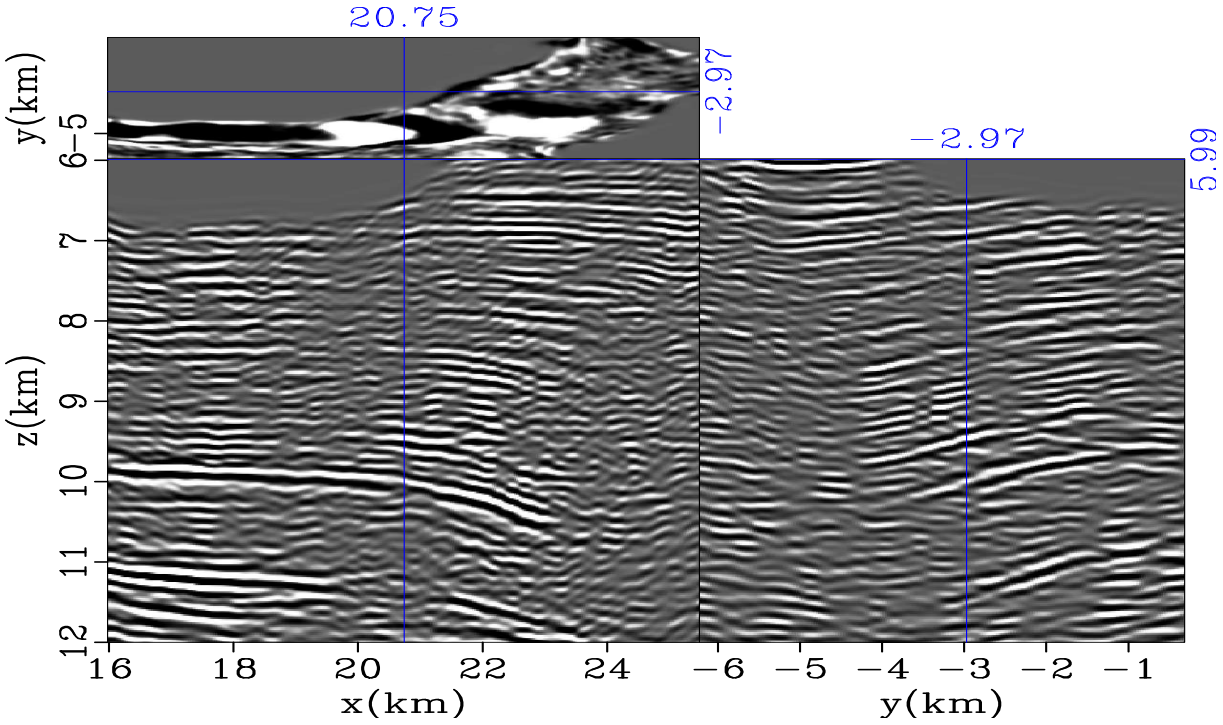

(b)

Figure 4: A close-up view at the target region. (a): the sediments-flooded starting velocity model, which is used for new data synthesis as well as the starting velocity model in later WEMVA inversion; (b): the zero subsurface-offset image of the ODCIG that we use for new data synthesis. We remove the salt reflection from the original ODCIG and apply inverse of diagonal Hessian matrix to the masked ODCIG for amplitude balancing. Compare this figure with figure 3. [**CR**]

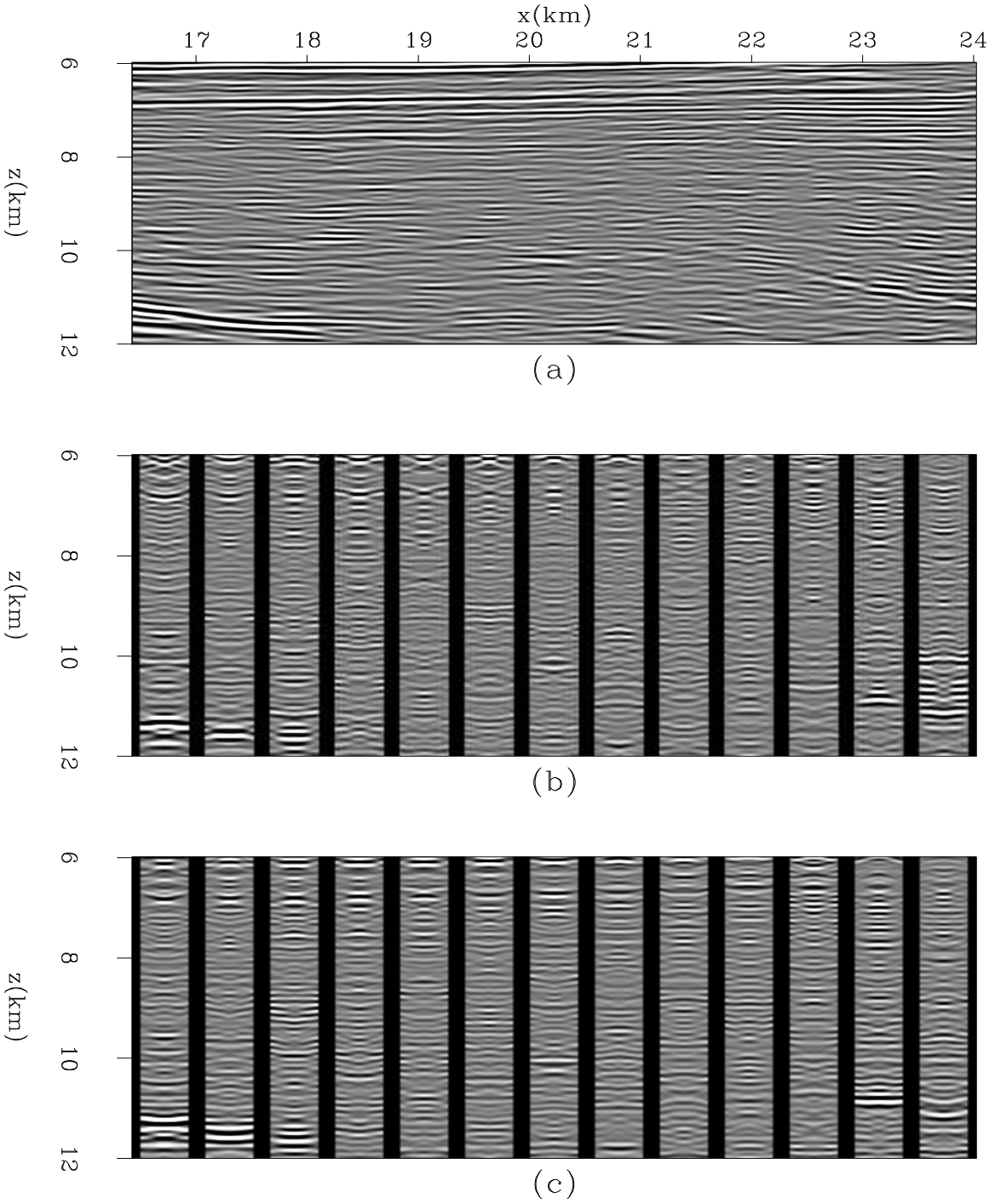

Figure 5: 3-D subsurface ODCIG in the target region, used as the input ODCIG for modeling the new data set. (a): An inline image section at $Y = -4.77\,\text{km}$; (b): the inline subsurface-offset (h_y is fixed at 0 km while h_x range spans $[-0.50\,\text{km}, +0.5\,\text{km}]$) CIG for different lateral locations in (a); (c): the crossline subsurface-offset (h_x is fixed at 0 km while h_y range spans $[-0.54\,\text{km}, +0.54\,\text{km}]$) CIG for different lateral locations in (a). [**CR**]

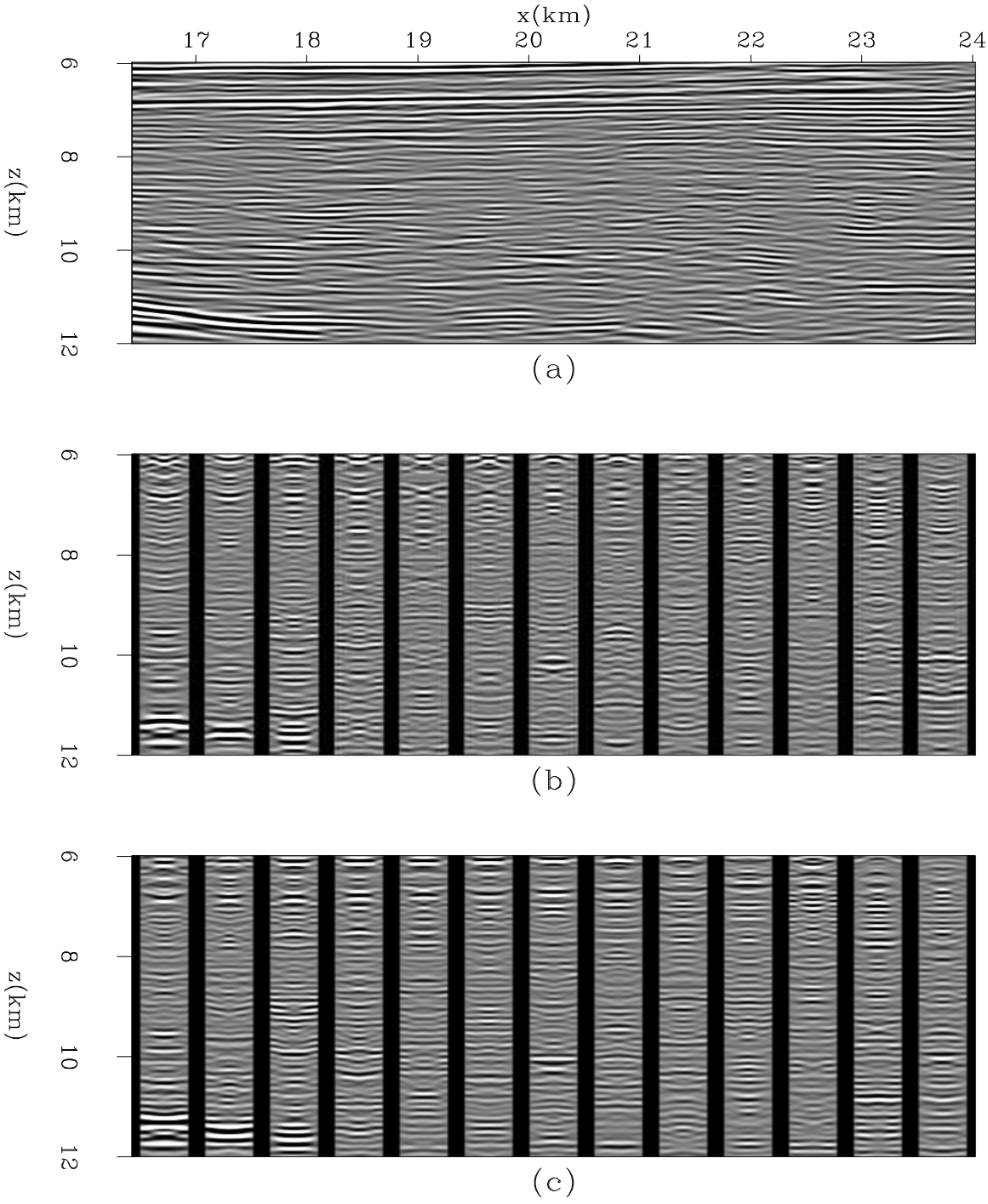

Figure 6: 3-D subsurface ODCIG in the target region, migrated using the generalized Born-modeling data set. Compare the figure with figure 5. (a): An inline image section at $Y = -4.77\,\text{km}$; (b): the inline subsurface-offset (h_y is fixed at $0\,\text{km}$ while h_x range spans $[-0.50\,\text{km}, +0.5\,\text{km}]$) CIG for different lateral locations in (a); (c): the crossline subsurface-offset (h_x is fixed at $0\,\text{km}$ while h_y range spans $[-0.54\,\text{km}, +0.54\,\text{km}]$) CIG for different lateral locations in (a). [**CR**]

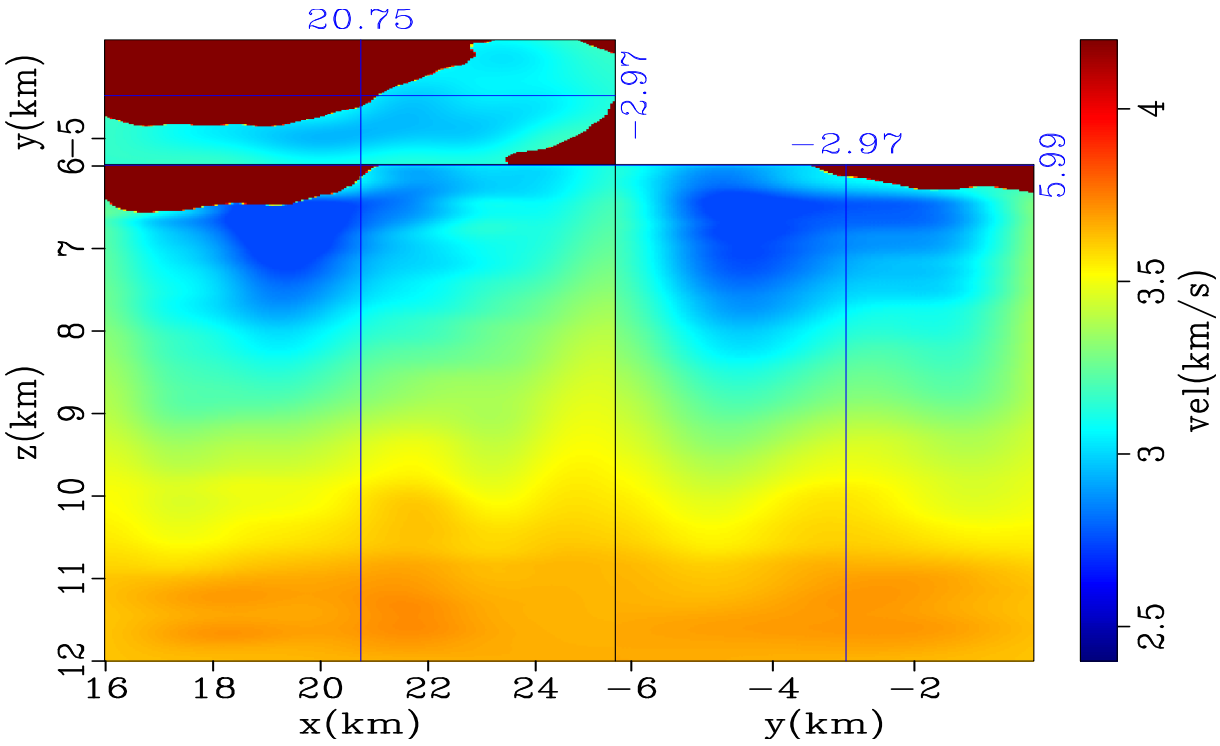

Figure 7: The inverted target region velocity model using the propose RMO-based WEMVA. The original salt area has been restored before plotting. Note the low velocity values immediately beneath the salt. [**CR**]

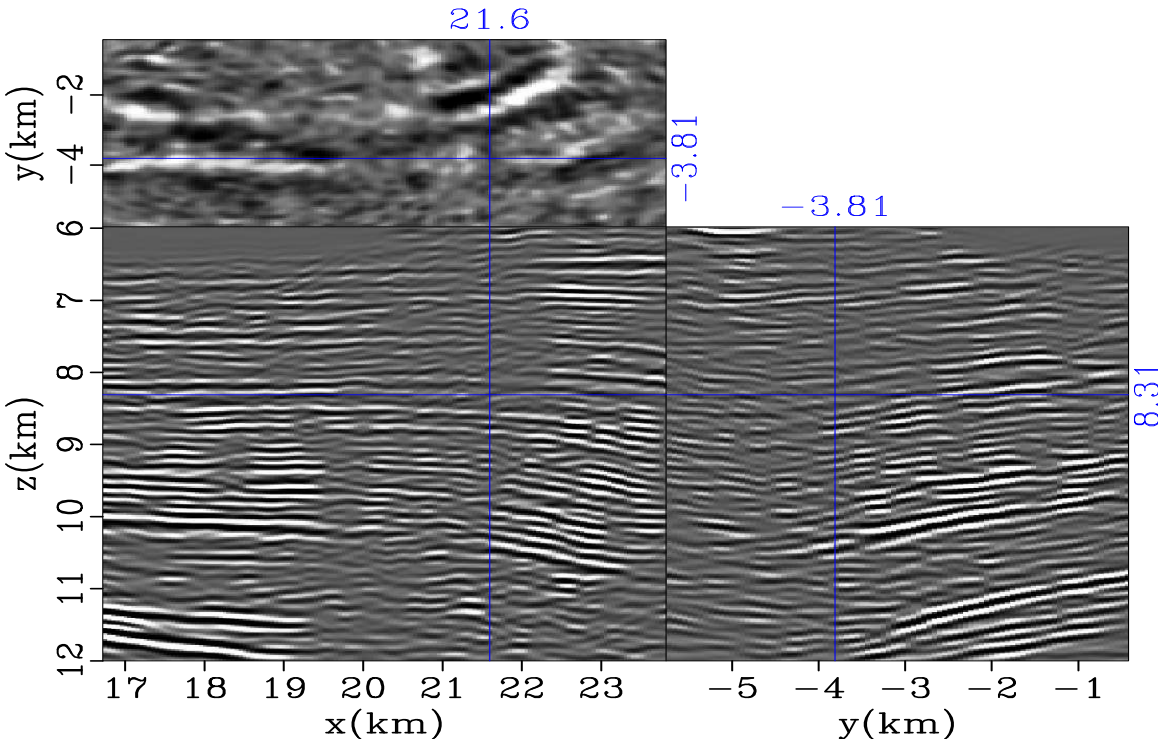

(a)

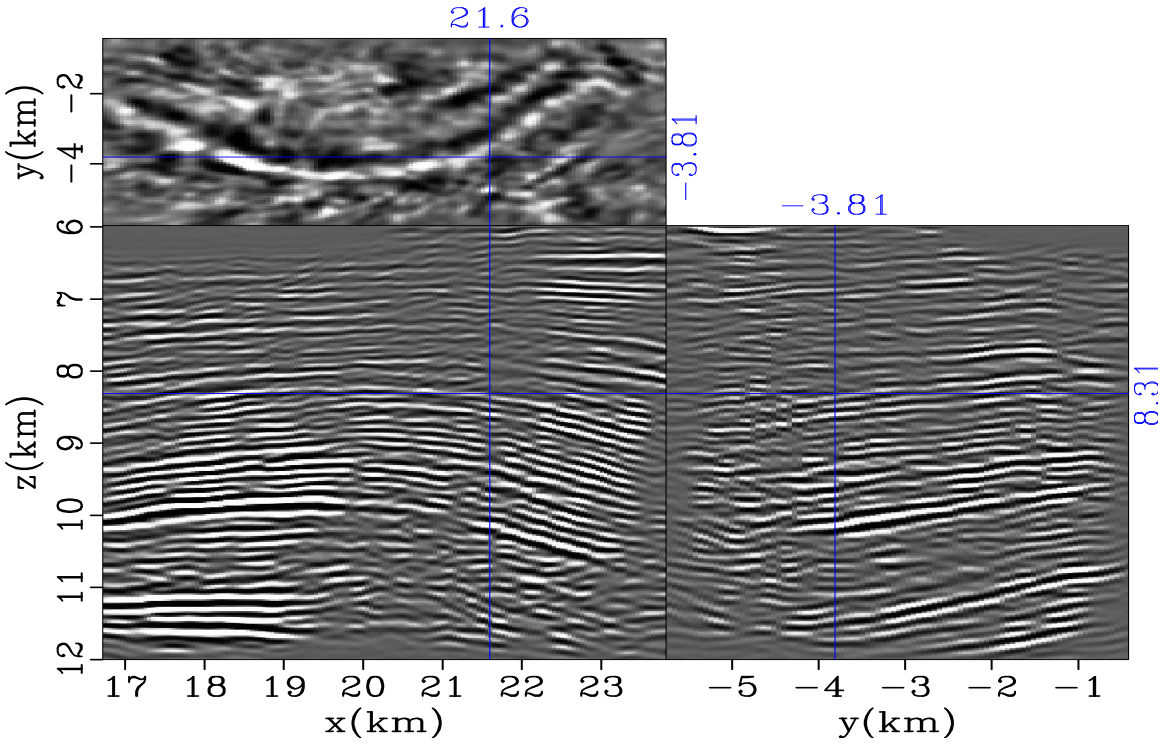

(b)

Figure 8: Three-panel view showing the comparison between the zero subsurface-offset images migrated with (a) the starting velocity model (figure 4(a)) and (b) the inverted velocity model (figure 7). The coordinates of each section are annotated in the figure. Both figures are plotted using the same clip value. [**CR**]

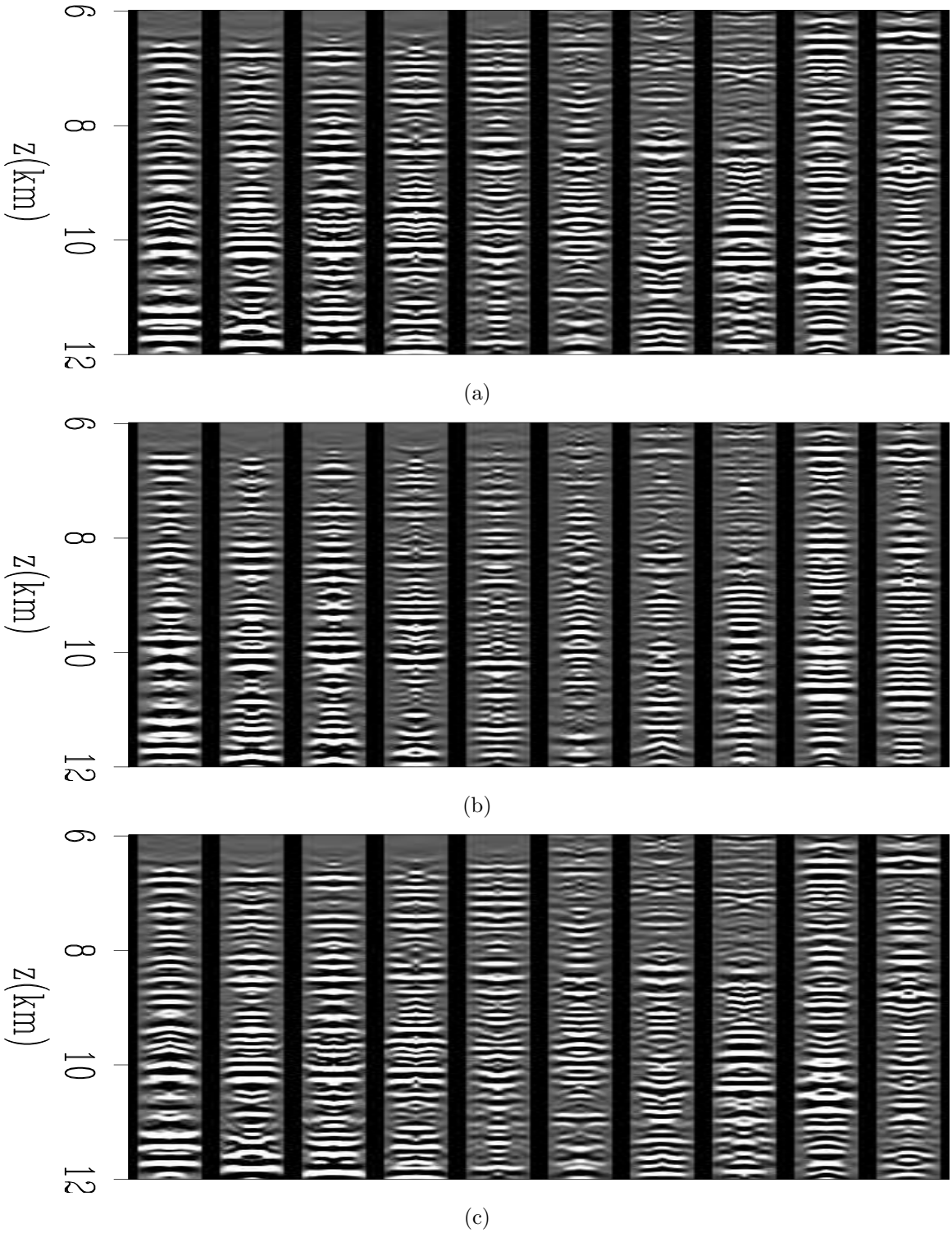

Figure 9: 3-D ADCIG migrated using the starting velocity model (figure 4(a)). The angle gathers are extracted from the same location where the X-Z image section in figure 8 is located. Each subplot shows the angle gathers at a certain azimuth for different lateral locations in X. The reflection angle range spans $[-25.0°, +25.0°]$. The three subplots ((a),(b) and (c)) show the angle gathers at $0°$, $-45.0°$ and $45.0°$ azimuth, respectively.

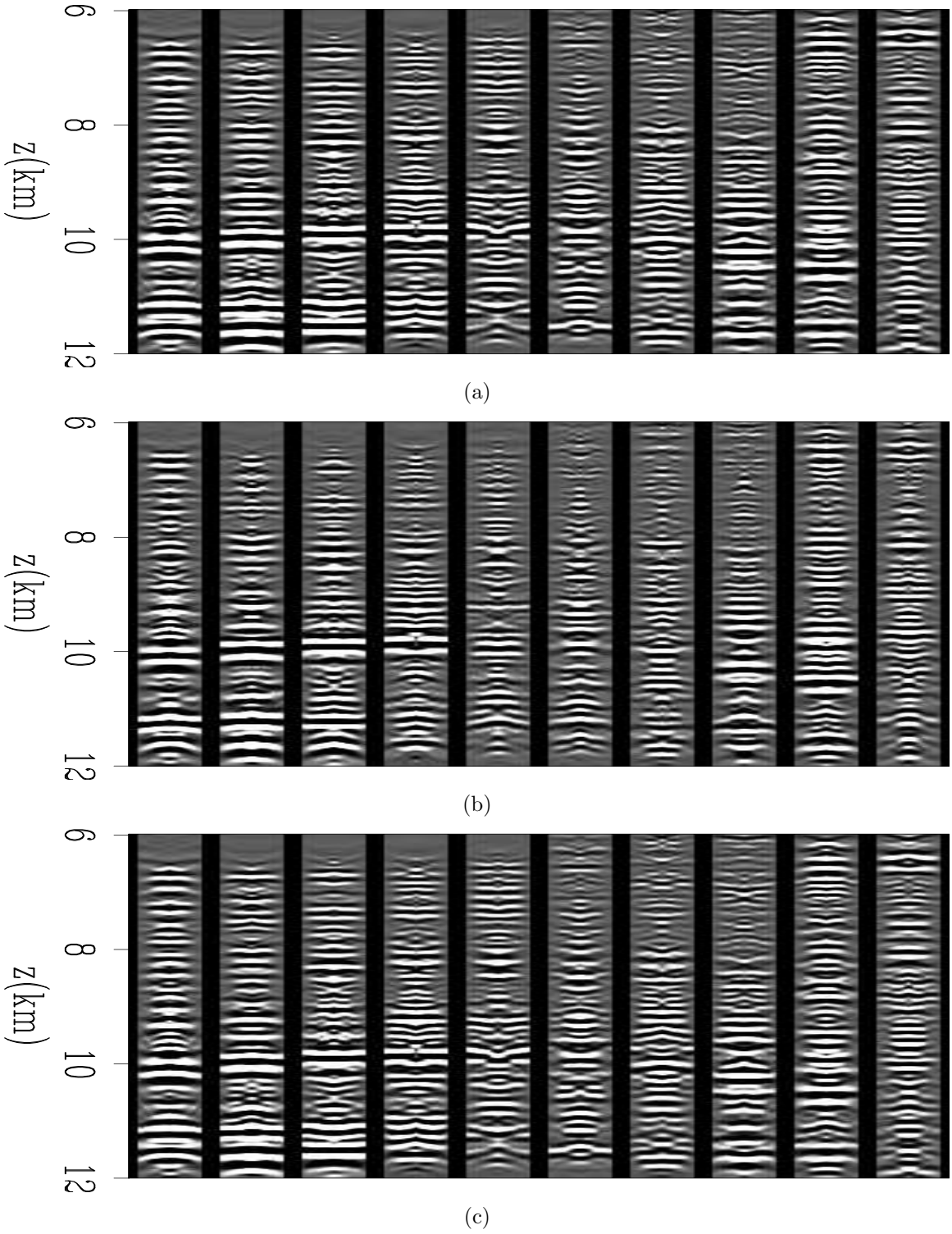

Figure 10: 3-D ADCIG migrated using the inverted velocity model (figure 7). The subplot description is the same as in figure 9. Compare this figure with figure 9.

nodes (as introduced by Biondi (1990)) to control the resolution of the inversion among iterations. By gradually increasing the number of spline nodes as the number of iterations increases, I constrain the inversion to resolve the low-wavenumber part of the model first, then gradually move up to a higher wavenumber to retrieve more model details. The initial spline nodes spacing is set as 1.5 km in X, 1.5 km in Y, and 0.3 km in Z, and the spacing reduces by ~ 0.1 km in X,Y and 0.02 km in Z for each iteration. When computing the model gradient, we use the aforementioned salt area mask to zero out any updates inside the salt. For the ADCIG sampling, we use 21 points along the reflection angle axis ranging from -25.0° to $+25.0^\circ$, and we compute 7 azimuths from -67.5° to $+67.5^\circ$.

Figure 7 shows the preliminary velocity estimation result we have obtained so far. For this result, Our RMO-based WEMVA inversion stopped improving after 5 iterations, and the objective function reduces by $\sim 5\%$ in total. An interesting point about the inverted velocity model is that the tomography is suggesting a low velocity zone beneath the salt body, and the lowest value in that zone is ~ 2650 km/s, which is $\sim 10\%$ lower than the initial velocity model.

To further verify that our inverted model is indeed improving the subsalt images, we plot the comparisons between the initial image and the image migrated using the inverted model, as shown in figure 8 and figure 11. To compare the image focusness, we use the same clip value for the initial image and the updated image. As we can see from both figures, the events of the updated image become more coherent, thus having higher amplitudes. Especially in figure 11 an anticline structure is formed because of the low velocity zone, and the continuity of those reflectors are also significantly improved. Figure 9 and 10 show the comparison between the ADCIG before and after update. The locations of these ADCIG are the slicing locations shown in figure 8. (In this example, it is the Z-X slice at $Y = -3.81$ km.) Similarly, figure 12 and 13 show the ADCIG comparison at a different location corresponding to figure 11. From these ADCIG comparisons, we can see that the majority of the ADCIG become more flat after velocity update, although there are certainly still some room for improvement even with the updated velocity.

CONCLUSION

We present a field data application of our target-oriented, RMO-based WEMVA tomography workflow using the E-Octopus III WAZ data set. The generalized Born-modeling based target-oriented approach we use enables huge computational savings, while preserving the velocity information in the original data losslessly. Although our current inversion result on a subsalt sediments region is preliminary, and the subsalt area is very challenging for velocity estimation; nonetheless, the inverted velocity model from our RMO-based WEMVA demonstrates convincing imaging improvement and uncovers an interesting low velocity zone beneath the salt, which might be worthy to investigate from geological aspects.

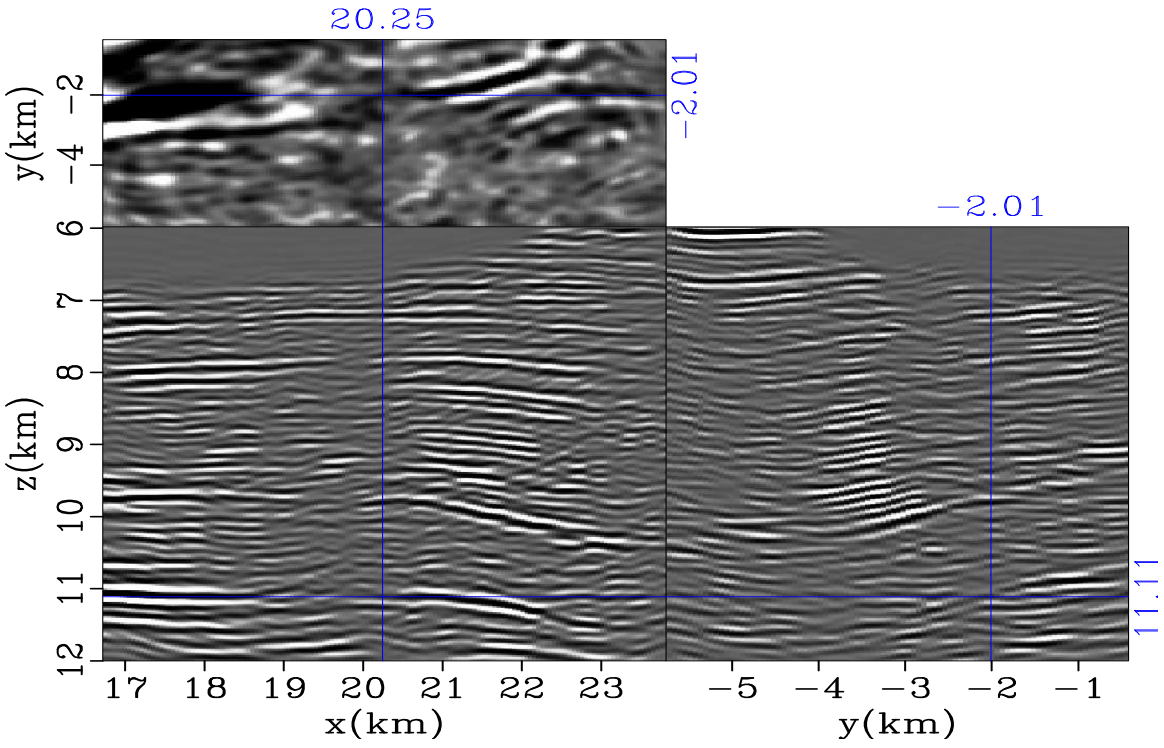

(a)

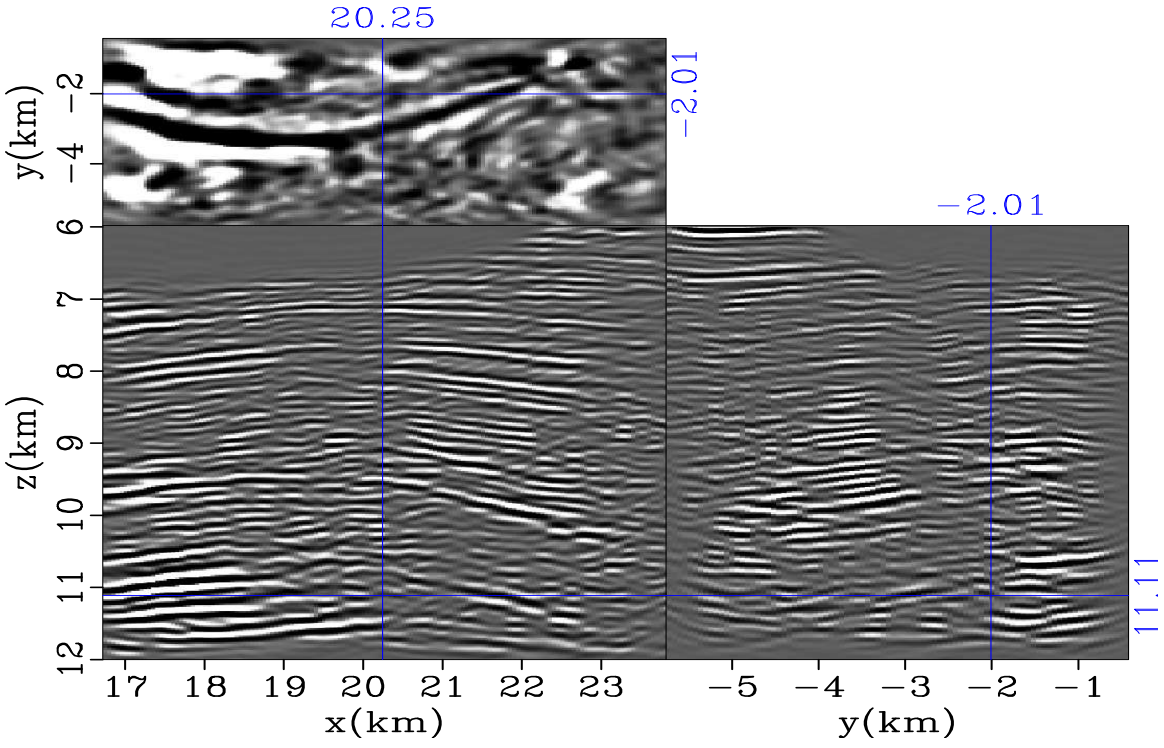

(b)

Figure 11: Another three-panel view showing the comparison between the zero subsurface-offset images migrated with (a) the starting velocity model (figure 4(a)) and (b) the inverted velocity model (figure 7). The coordinates of each section are annotated in the figure. Both figures are plotted using the same clip value. [**CR**]

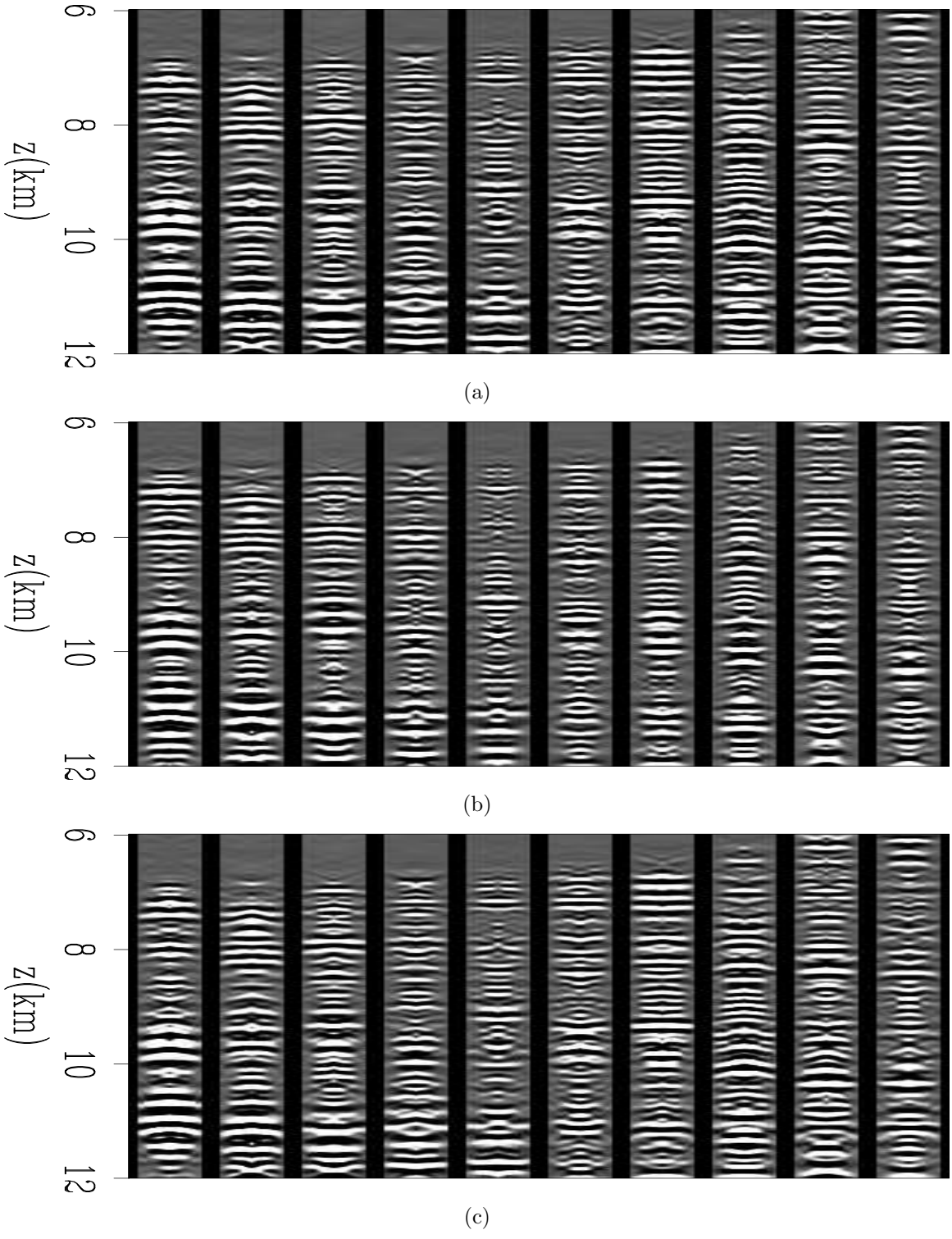

Figure 12: Same description as in figure 9, other than that the locations of these angle gathers are from the X-Z image section in figure 11. [**CR**]

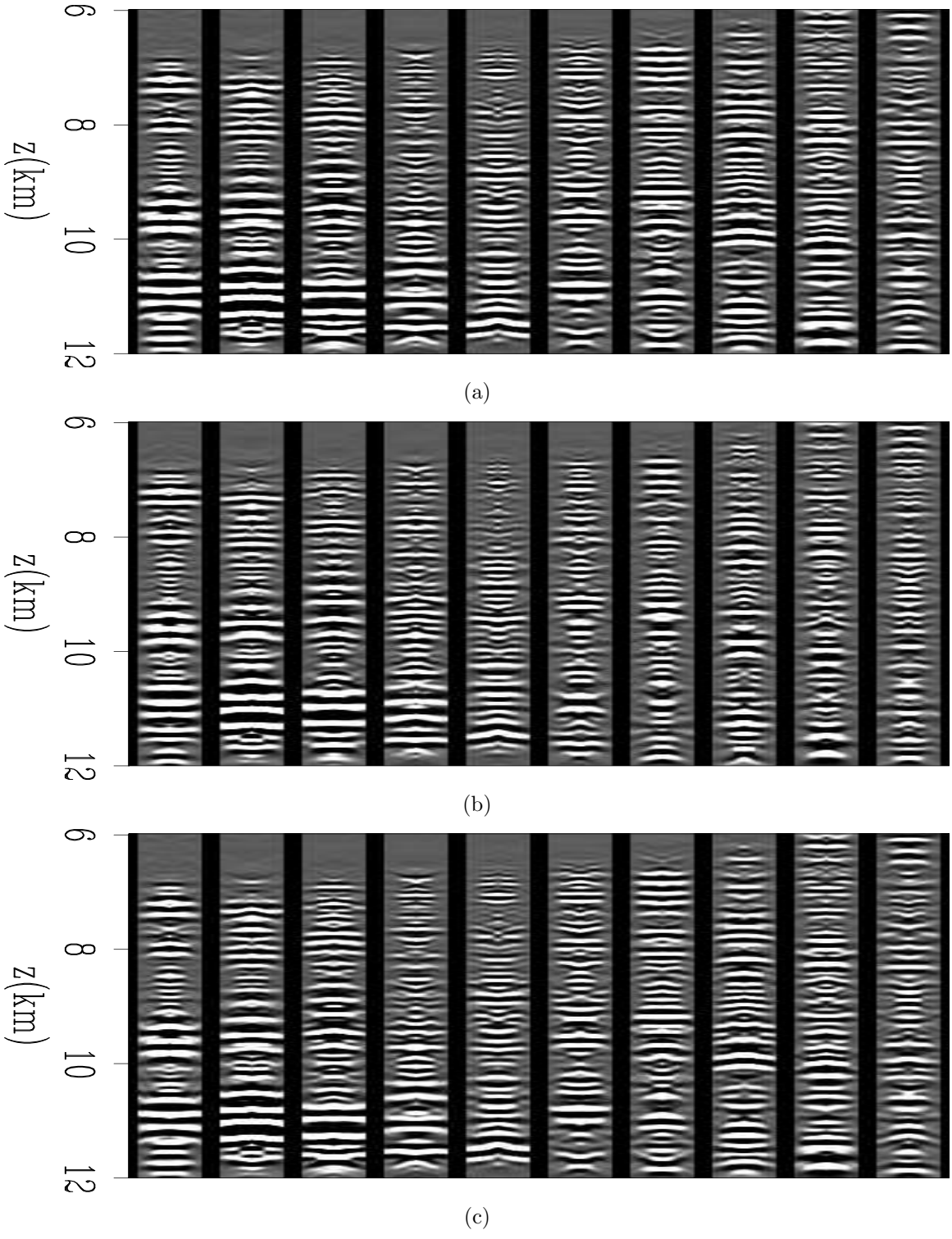

Figure 13: Same description as in figure 10, other than that the locations of these angle gathers are from the X-Z image section in figure 11. Compare this figure with figure 12. [**CR**]

ACKNOWLEDGMENT

We thank Schlumberger for providing the E-octopus III data set used in this study.

APPENDIX A

AUTOMATIC EVENT DETECTION

In this appendix, we explain how we implement the automatic event detection module for the gradient calculation in the RMO-based WEMVA method.

Anchor points detection

The basic idea for our anchor point detection workflow is inspired by the methodology proposed in Cullison (2011). First our method uses several image processing techniques to extract all potential event anchor point candidates, and then filter out a portion of candidates based on several geophysical criteria before outputting the final set of anchor points. Let me denote the stacked image (zero subsurface offset image) $I(z, x)$. To find candidate anchor points, I perform the following steps:

1. Apply 1-D (along z axis) automatic gain control (AGC) to the stacked image $I_{bal}(z, x)$, in order to broadly balance the amplitude of reflectors in the image.
2. Take the energy envelope (magnitude of the input's Hilbert signal) along z axis on $I_{bal}(z, x)$, denoting the output as $I_E(z, x)$.
3. Apply *non-maximum suppression* (along z axis) to $I_E(z, x)$. As its name suggests, non-maximum suppression will suppress all samples that are not local maxima in the input image to zero. It will produce a binary image of the input size, and only the locations of local maxima in the input image are set to 1, while all the rest of the output are set to 0. From this binary image, I extract the locations of all non-zero values and place them in the candidates set of the anchor points, S_{cand}.

However, not all candidate points in S_{cand} are well-suited for WEMVA gradient back-projection. In other words, extra quality check (QC) is helpful to prevent noisy data going to the gradient calculation. Specifically, our implementation filters out any candidate points if they do not meet one of the criteria below:

1. Because the assumption of specular reflection is the theoretic foundation of all reflection tomography methods, I screen out all candidate points that do not satisfy specular reflection requirement. I achieve this screening by computing

linearity coefficients over all candidate points and threshold the values of linearity coefficients.

First introduced into the field of exploration Geophysics by Hale (2009a,b), the *linearity coefficient* is a good measure to quantify how specular a reflection point is. Briefly speaking, if the linear coefficient of the target reflection point is high (close to 1.0), it indicates that there is a strong local linear reflector structure around that point. Thus, we know that the specular reflector assumption holds well. Similarly, if the linear coefficient is low (close to 0.0), it indicates that there is no locally linear reflector structure around that point (for example, the target point is on fault boundary, or is just an isolated diffractor). Therefore, the specular reflector assumption does not hold.

The local linearity coefficients of the stacked image can be conveniently estimated using structure tensor (Cullison, 2011).

2. I also filter out candidate points that have a large dipping angle, because neither the theory nor the way that I compute gathers handles steeply dipping reflectors well. The reason is explained as follows:

   - In the theoretic aspect, our derivation assumes that the ADCIG shift only vertically under velocity perturbation. In the case of reflector dips being large, this vertical shift assumption will be challenged because it is more accurate to assume each angle-domain gather shifts along the normal direction (perpendicular to the corresponding dipping interface).
   - On the implementation side, note that I compute the ADCIG indirectly by converting from subsurface offset common image gathers (Sava and Fomel, 2003). The horizontal subsurface offset (h_x) common image gathers are known to lose resolution and accuracy for angle-domain gathers on steeply dipping reflectors (Biondi, 2006).

   Therefore our workflow also filters out steep reflectors. As for how to determine the steepness of reflectors, we can conveniently estimate local dipping angles of the stacked image using structure tensors as well (Cullison, 2011).

Variable event window size

After I identify the set of event anchor points, I can further detect the actual window size of each event instead of using a pre-set constant window size universally:

1. For each anchor point, extract the amplitude at that anchor location from the energy envelope image $I_E(z, x)$.
2. We can infer that each anchor point positions approximately at the center of the event it belongs to, because the anchor point samples the peak amplitude of the energy envelope. Therefore our code starts from the anchor point's location, then searches in both directions ($\pm z$) for the tails of the energy envelope.

Illustrative example on automatic event detection

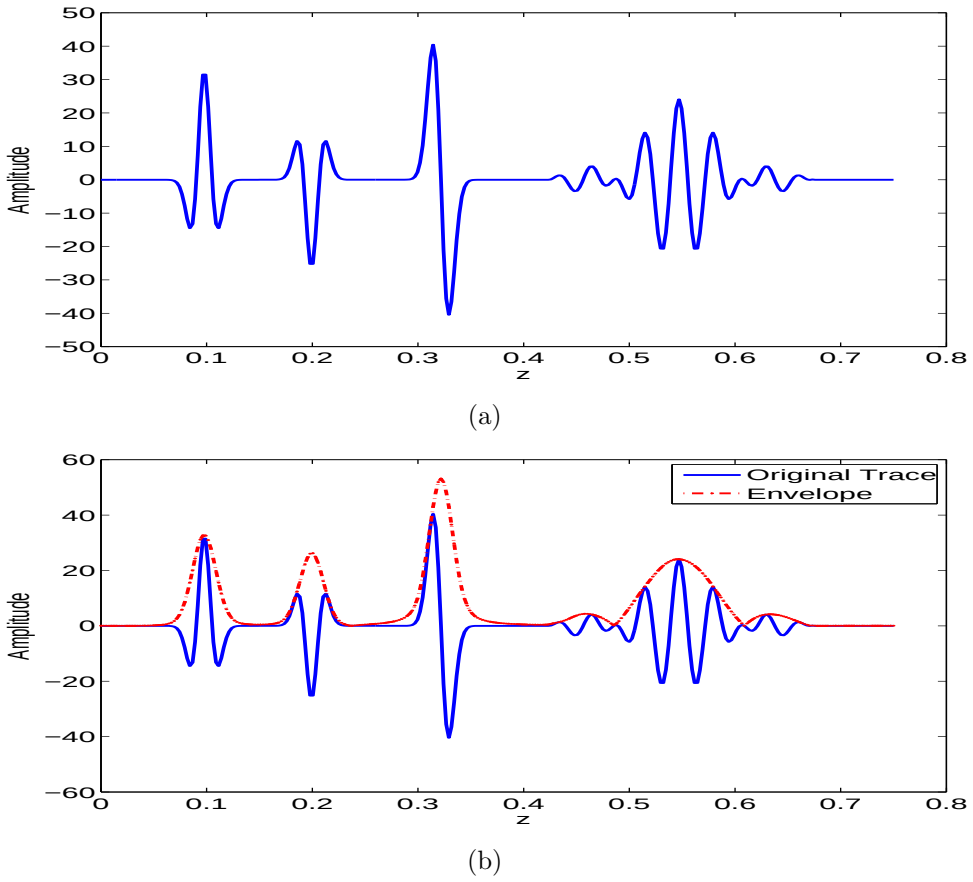

Figure A-1: An example to illustrate the event detection workflow. (a): the input 1-D signal; (b): the input with its energy envelop overlaid. [**CR**]

As an intuitive explanation for the algorithms used in our automatic event detection module, I present a simplified event detection example on a 1-D seismic trace input. In the RMO-based WEMVA case, we can think of the input as an image trace along the depth direction at a certain horizontal location, $I(z, x = x_0, y = y_0)$.

Figure A-1(a) shows the input 1-D signal. The goal is to detect the individual events accurately and efficiently. As we can visually identify from the plot, I deliberately create 4 distinct events in the input, each with a different signature (waveform):

1. A typical Ricker2 wavelet (second derivative of Gaussian).
2. A Ricker2 wavelet with opposite polarity.
3. A Ricker1 wavelet (first derivative of Gaussian). This wavelet is asymmetric and has a 90° phase difference compared to the Ricker2 wavelet.

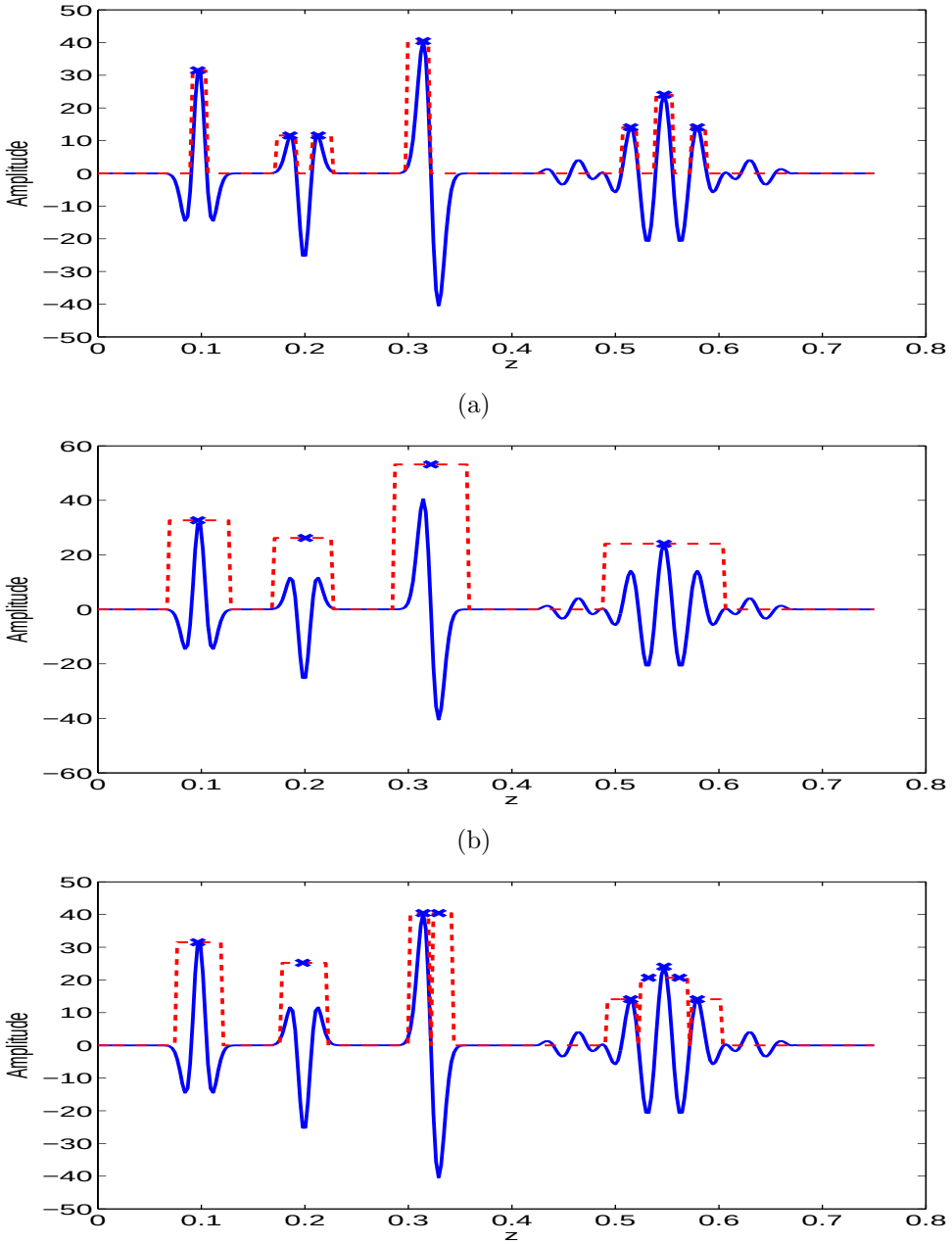

Figure A-2: The results of detected anchor points(shown as $\times$ marks) and event windows (shown as dash lines) using different inputs: (a) the original signal as input; (b) the energy envelope as input; (c) the absolute value of the original signal as input. [**CR**]

4. A typical Ormsby wavelet (Ryan, 1994). This wavelet usually has bigger side lobes (more rippling) compared to the Ricker wavelet due to the steeper tapering effect on the edges of the spectrum.

These events possess different signal characteristics (variant amplitude, polarity, phase and spectrum shape) that help to demonstrate the merits of the proposed approach.

Figure A-1(b) shows the energy envelope overlaying the input. As we can see, the envelope strips out many of the complexities in the original signal (like asymmetric phase, negative polarity, vibrating waveform, etc.), and singles out the "wave packet" information for each event. The simplicity brought by the energy envelope makes it a much better choice for anchor point detection than the original signal, as demonstrated by the following example.

Figure A-2 shows the anchor points found by applying non-maximum suppression to different input signals. More specifically, figure A-2(a) uses the original signal as detection input, and figure A-2(b) uses the energy envelope. For comparison, I add the result using the absolute value of the original signal as input, shown in figure A-2(c). Apparently, the result using the energy envelope (figure A-2(b)) is the most accurate. The result in figure A-2(a) fails on the second event that has a negative polarity. Because of this negative polarity, the two local maxima it finds are indeed the peaks of two side lobes rather than the main lobe. This result also fails on the last event due to the severely vibrating waveform, that the computer program picks up both the peak of main lobe and the first two strong side lobes. The result in figure A-2(c) is able to handle negative polarity in the second event because it uses the absolute value of the original signal as input. However, it fails on the third and fourth event. The result contains several false positives because the absolute value function converts local minima into local maxima.

After the event anchor points are located, figure A-2 also shows the detected event window sizes of every anchor point for each corresponding test case. The detected event windows are drawn as box functions with dash lines. As the figure indicates, the result using energy envelope is the most accurate.

REFERENCES

Biondi, B., 1990, Seismic velocity estimation by beam stack: PhD thesis, Stanford University.

Biondi, B. L., 2006, 3-D Seismic Imaging.

Cullison, T. A., 2011, An image-guided method for automatically picking common-image-point gather locations from seismic images: Master's thesis, Colorado School of Mines.

Hale, D., 2009a, Image-guided blended neighbor interpolation of scattered data: 1127–1131.

———, 2009b, Structure-oriented smoothing and semblance: CWP-Report, **635**, 261–270.

Li, Y., 2014, Wave-equation migration velocity analysis for VTI models with geological and rock physics constraints: PhD thesis, Stanford University.

Ryan, H., 1994, Ricker, Ormsby; Klauder, Butterworth - A choice of wavelets: CSEG Recorder, **19**, 8–9.

Sava, P. C. and S. Fomel, 2003, Angle-domain common-image gathers by wavefield continuation methods: Geophysics, **68**, 1065–1074.

Tang, Y., 2011, Imaging and velocity analysis by target-oriented wavefield inversion: PhD thesis, Stanford University.

Zhang, Y., 2015, Velocity model building using residual-moveout-based wave-equation migration velocity analysis: PhD thesis, Stanford University, (to be published).

Zhang, Y. and B. Biondi, 2013, Moveout-based wave-equation migration velocity analysis: GEOPHYSICS, **78**, U31–U39.

———, 2014, Residual-moveout-based WEMVA: A WAZ field data example - Part I : SEP-Report, **152**, 223–238.

Zhang, Y., B. Biondi, and R. Clapp, 2013, Accelerating residual-moveout-based wave-equation migration velocity analysis with compressed-sensing: SEP-Report, **149**, 95–106.